Electromechanical study of graphene reinforced lead-free functionally graded tile for vibration energy harvesting

Jitendra Adhikari[1] (iD)**, Rajeev Kumar[1], Vikas Narain[2] and Satish Chandra Jain[1]**

Abstract

This study focuses on the electromechanical analysis of functionally graded graphene reinforced piezoelectric composite (FG-GRPC) structures in order to identify circuit metrics such as voltage and power. The graphene platelets (GPLs) scatter evenly and parallelly in each graphene platelets reinforced piezoelectric composite (GRPC) tile. The effective modulus of elasticity for the GRPC tile is calculated by the Halpin-Tsai (HT) parallel model. The rule of the mixture (ROM) is employed to estimate the effective mass density, poisson's ratio, and piezoelectric properties of GRPC structure. A simple power law distribution is responsible for the spatial disparity in composition over the thickness to generate FG-GRPC structural tiles. The first-order shear deformation theory and Hamilton's principle are used to derive the governing finite element equations for the FG-GRPC plates. The impact of external resistance, frequency, volume fraction, piezoelectric characteristics, and geometry of the tile on the circuit metrics of FG-GRPC structures are thoroughly examined. Our results reveal that the circuit metrics of FG-GRPC plates are significantly enhanced due to consideration of material grading exponent and a small quantity of GPLs. This article will provide the necessary physical insights for modeling the electromechanical coupling in multipurpose piezoelectric materials, devices, and large-scale systems, allowing them to be used in industrial applications such as pressure sensors, miniature ultrasonic motors, fuel injectors, active controllers, and robotic systems.

1. Introduction

1.1. State of art review

As we advance toward the next industrial revolution, big data, Internet of Things, and artificial intelligence have increased our reliance on wireless communication and technological devices (Shi et al., 2020; Tien, 2017). These burgeoning sectors are reshaping virtually every area of our lives. Energy storage research is becoming increasingly vital as the majority of the current gadgets are battery-powered. While each electronic gadget consumes a little amount of energy, the aggregate number of devices is enormous (Agnolucci, 2007). These devices are powered by batteries, and it is highly improbable that all of these gadgets will be powered by batteries, as each battery must be identified, examined, and replaced on a regular basis (Shirvanimoghaddam et al., 2019). In this circumstance, one possibility is to harvest energy

from the environment where devices are positioned. Numerous strategies for effective environment energy harvesting have been thoroughly explored, particularly triboelectricity (Kumar et al., 2022) and piezoelectricity. Because of the widespread availability of ambient mechanical energy in the form of vibrations, motions, and noises, energy harvesting through piezoelectric materials has sparked considerable interest (Singh et al., 2021). However, the fragile nature of

[1]School of Engineering, Indian Institute of Technology Mandi, Mandi, Himachal Pradesh, India
[2]Shri Bhawani Niketan Institute of Technology and Management, Jaipur, Rajasthan, India

Corresponding author:
Jitendra Adhikari, School of Engineering, Indian Institute of Technology Mandi, Mandi, Himachal Pradesh 175005, India.
Email: jitendraadhikari42@gmail.com

piezoceramic material prohibits its usage in various electronic devices (Adhikari et al., 2022). In this scenario, piezoelectric composites with improved performance based on graphene nano platelet reinforcement may be the best option. Graphene is a single-atom thick carbon sheet with exceptional electronic, mechanical, and thermal properties, made up of a honeycomb crystal arrangement of strong carbon bonds (Lu et al., 2006). Since Novoselov reported their lab research on graphene in 2004, the material has been attracting a lot of attention from engineers and researchers (Geim and Novoselov, 2010). Furthermore, graphene has an elastic modulus of 1 TPa and an intrinsic strength of up to 130 GPa (Zaman et al., 2011), both of which are substantially greater than those of traditional materials and fiber composites. Because the low filler content improves the characteristics of metals, ceramics, and polymers, GPL reinforced composites are being used in a variety of scientific applications (Layek et al., 2010; Rafiee et al., 2009). This is accomplished by the selective incorporation of GPLs into the material matrix, which dramatically improves the composite's performance. This has been demonstrated experimentally by Rafiee et al. (2009), who discovered that adding 0.1% weight fraction of GPLs raises the effective elastic modulus of graphene reinforced epoxy nanocomposites by 131%. Likewise, the electrical conductivity of the epoxy resin/graphite nanocomposites is substantially increased by a factor of 12 (Lu et al., 2006). Numerous theoretical and experimental research indicated that graphene-polymer nanocomposites might be used to improve the mechanical capabilities of equipment in the automotive, aerospace, and civil engineering domains.

On the other hand, functionally graded material (FGM) is a kind of non-uniform composite material that may be made to fulfill a variety of engineering needs by continually modifying the material composition. Various approaches for evaluating the vibrational behavior of functionally graded (FG) plates have been devised in the past. Instances include a three-dimensional (3D) elastic solution proposed by Vel and Batra (2000) to analyze multi-layered piezoelectric plates under random constraints by using Eshelby-Stroh formulation. Next, Sankar (2001) introduced 3D exact solutions for functionally graded beams under mechanical pressure.. The dynamic properties of FGM plates in a thermal environment were studied by Sundararajan et al. (2005) using a variety of parameters such as the gradient index, temperature, thickness and aspect ratios, and skew angle. According to Roque et al. (2007), the free vibration of FGM sheets with numerous boundary conditions can be studied using the radial basis function method. Following that, Malekzadeh and Alibeygi Beni (2010) used the FSDT to investigate the free vibration of a FGM plate with a certain boundary condition under a thermal environment. Using thin plate theory, He and his colleagues developed the finite element framework to control the shape and vibration of FGM plates with integrated piezoelectric sensors and actuators under mechanical loads (He et al., 2001).

Numerous research groups have concentrated on the buckling, linear and nonlinear vibration, bending, and dynamic behaviors of beams and plates. For instance, Zhu et al. (2018) examined the nonlinear dynamical behavioral responses of the viscoelastic sandwich beam. Using a mechanical degradation model, Wang and Wang (2018) performed the buckling and vibration simulation on natural fiber reinforced composites. Now for the case of graphene platelets, Yang Kitipornchai and their group (Feng et al., 2017; Song et al., 2017; Wu et al., 2018) examined the vibration behavior of graphene platelet reinforced structures. GPL-reinforced micro-beams, micro-plates, and micro-shells were explored by Sahmani and Aghdam (2017) using nonlocal strain gradient theory. Using cylindrical panels or plates as models, Zhang et al. (2020) examined the buckling and vibration properties of GPL-reinforced pretwisted blades. Later, Gholami and Ansari (2018) investigated the geometrically nonlinear harmonically stimulated vibration of GPL reinforced composite plates with varying edge conditions using third-order shear deformation theory. Song et al. (2020) studied the nonlinear dynamic instability in FG-GRC beams with edge fractured conditions made up of completely bonded layers. Results indicate that as geometric nonlinearity rises, the principle unstable zones become more constrained and shift to higher excitation frequencies. Another recent study by his group (Song et al., 2022) looks into the nonlinear vibration response of hybrid edge-cracked beams strengthened by GPLs, which were arranged on a two-parameter elastic basis with thermal settings. Wu et al. (2022) provides an FSDT-based free vibration analysis of partially submerged beams made of FG-GRC. The findings shows that the first order vibration mode is barely affected by the beam-fluid interaction, whereas the fundamental frequency is reduced significantly. By using the finite element approach, Rout et al. (2019) investigated GPL reinforced single and double curved composite panels in thermal conditions. Wang et al. (2019) analyzed the free vibration properties of metal foam cylindrical shells and microshells strengthened by GPLs using Donnell nonlinear shell theory. Next, Zhao and colleagues used the finite element technique to investigate trapezoidal structures strengthened with GPLs' linear and nonlinear bending performance (Zhao et al., 2017). Recently, Yang and co-workers (Yang et al., 2017, 2018) established the notion of functionally graded materials into the concept design of graphene-based composites. They proposed multilayer FG-GPRC, inside which GPLs are completely random and evenly dispersed in each layer, while the weight fraction of each GPL varies layer-by-layer. Additionally, they

conducted a number of illuminating investigations on the dynamic behaviors of FG-GRPC structures utilizing analytical methods, finite element analysis, and molecular dynamics modeling. Further, Shen and his teammates (Shen et al., 2018) showed improved dynamic behaviors of FG-GRPC when thermal conditions were taken into account.

1.2. Novelty of the article

Based on a thorough assessment of the literature, it is clear that the majority of current studies have used analytical methods and numerical approaches to examine mechanical and thermal loads for buckling and bending analysis. Some papers, such as Wu et al. (2018) documented the linearity of FG-GRPC structures, whereas others, such as Yang et al. (2018) and Shen et al. (2018) investigated the non-linearity of FG-GRPC structures. However, to the best of the authors' knowledge, the electro mechanical investigation of FG-GRPC tile employing circuit analysis remains an untapped field of research. Additionally, almost all of the mentioned research refers to the U-O-X-V distribution patterns of GPLs in a single material as FG-GRPC. On the other hand, we established FG-GRPC in our current study using two different GRPC materials whose properties vary via a simple power law distribution. In the current study, two lead free piezoelectric materials namely Barium Titanate (BaTiO$_3$) and -(C$_2$H$_2$F$_2$)$_n$- (PVDF) are reinforced with graphene and their mechanical and electrical characteristics are determined using HT and ROM. The implications of the GPLs volume fraction in a piezoelectric plate acting as an energy harvester are explored for both lead free materials. Following that, the properties of both reinforced composites are functionally graded using power law to create the lead-free FG-GRPC tile. The present work employs first-order shear deformation theory and Hamilton's principle to obtain the governing finite element equations for the FG-GRPC tile. An exhaustive parametric analysis of the effect of frequency, external resistance, material grading exponent, side to thickness ratio, and piezoelectric thickness on the circuit metrics, namely voltage and power, is also explored. Figure 1 displays the overall structure and flowchart of our study to obtain the electromechanical behavior of the FG-GRPC structure.

2. Theoretical formulation

2.1. Graphene reinforced piezoelectric composite (GRPC)

Graphene additions have the potential to significantly improve the piezoelectric, mechanical, and stiffness characteristics of piezoelectric matrix composite materials. The GPL nanofillers are distributed evenly across each GRPC surface and exhibit layer-wise diversity throughout the material's thickness. The HT and Mori-Tanaka models are adequate to estimate the modulus and stiffness of the composites containing 2D nanofillers of GPLs (Layek et al., 2010; Mao and Zhang, 2018). However, when the volume fraction of graphene reinforcement in the piezoelectric matrix is less than 1%, the HT parallel method is appropriate for calculating the modulus of elasticity (Layek et al., 2010). As a result, we use the HT model in our research to perform an electromechanical investigation of a GRPC with a volume fraction of graphene less than 1%.

The effective modulus of elasticity for the GRPC layer is (Layek et al., 2010)

$$Y_c = \frac{1 + \frac{2l_{gpl}}{3t_{gpl}} \eta_L V_{gpl}}{1 - \eta_L V_{gpl}} Y_M \qquad (1)$$

Where

$$\eta_L = \frac{\frac{Y_G}{Y_M} - 1}{\frac{Y_G}{Y_M} + \frac{2l_{gpl}}{3t_{gpl}}} \qquad (2)$$

l_{gpl}, V_{gpl}, and t_{gpl} respectively represent the length, volume fraction and thickness of the rectangular GPLs, and the subscripts "M" and "G" respectively represent the piezoelectric matrix and the GPLs.

The Poisson's ratio ν, the density ρ, the piezoelectric constant e_{pq}, and the material permittivity κ_{pq} of the piezoelectric layer are calculated by the ROM and are defined as (Mao and Zhang, 2018, 2019).

$$\nu = \nu_G V_{gpl} + \nu_M (1 - V_{gpl}) \qquad (3)$$

$$\rho = \rho_G V_{gpl} + \rho_M (1 - V_{gpl}) \qquad (4)$$

$$e_{33} = e_{33,G} V_{gpl} + e_{33,M} (1 - V_{gpl}) \qquad (5)$$

$$\kappa_{pq} = \kappa_{33,G} V_{gpl} + \kappa_{33,M} (1 - V_{gpl}) \qquad (6)$$

2.2. Functionally graded graphene reinforced piezoelectric composite (FG-GRPC) material

FG-GRPC is a kind of GRPC material which can be designed to meet various engineering requirements by changing the properties continuously throughout the height. These chemical, physical, or mechanical properties include density, piezoelectric coefficient, poisson's ratio, dielectric coefficient, and modulus of elasticity.

The FG-GRPC's features vary uniformly from bottom to top surface, as per the simple power law distribution (He et al., 2002).

$$\varphi_c = \left(\frac{1}{2} + \frac{j}{h} \right)^m \qquad (7)$$

where φ_c and h are the volume fraction of the properties and thickness of layer, respectively j is the distance from the neutral axis to a point where the volume
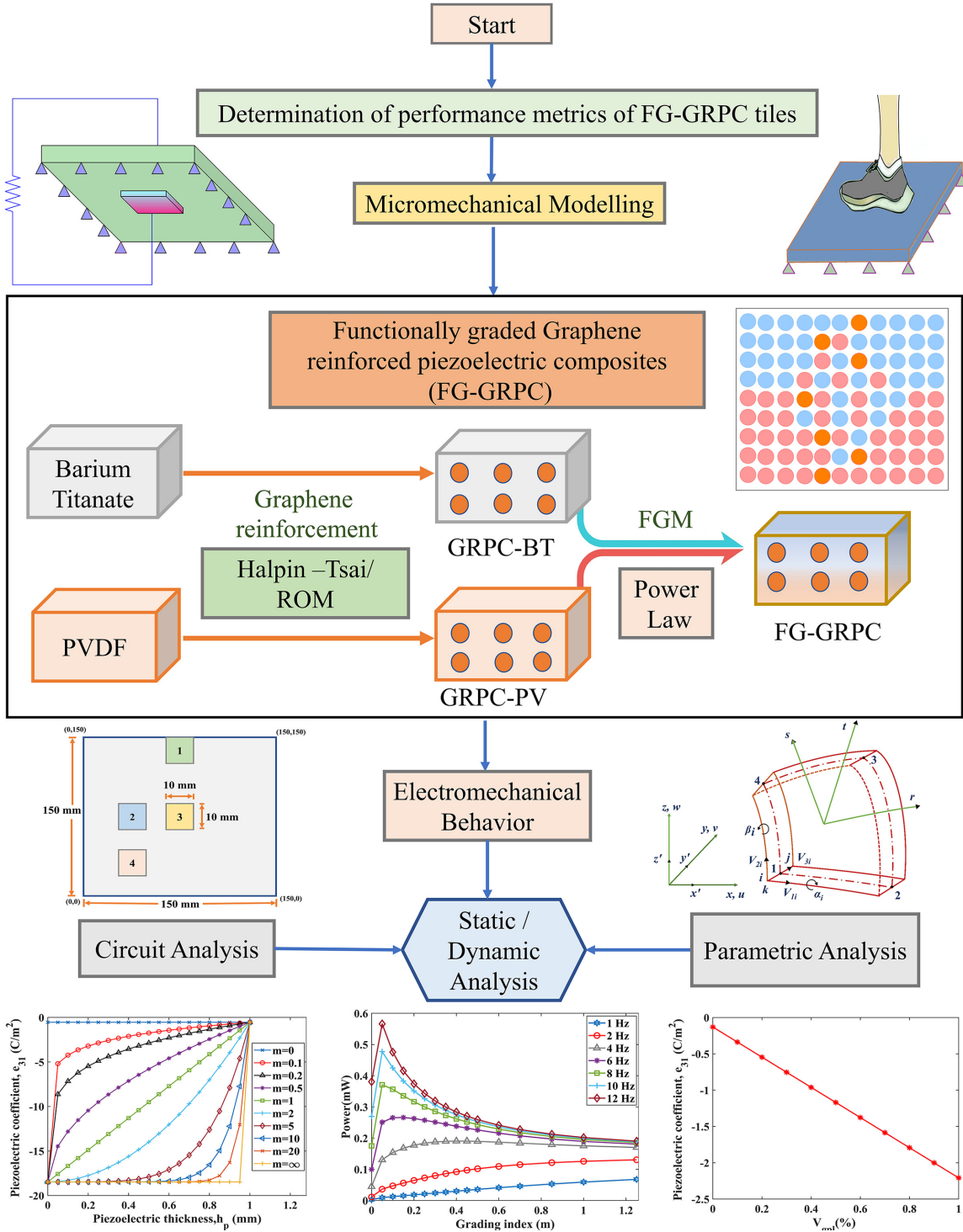
Figure 1. The detailed flowchart describing electromechanical study of FG-GPRC structure.

fraction needs to be calculated, and *m* is the material grading exponent which varies from 0 to ∞.

The effective properties of FG-GRPC patch along the thickness is given as (He et al., 2002).

$$P_{eff}(j) = P_T \varphi_T(j) + P_B(1 - \varphi_T(j)) \qquad (8)$$

$$\varphi_T + \varphi_B = 1 \qquad (9)$$

where *B* and *T* are subscripts for bottom and top layers, respectively. φ and *P* are the volume fraction and property of FG-GRPC, respectively. P_{eff} is the effective property of FG-GRPC. Now, using equations (7) and (8), property variation in FG-GRPC is given as

$$e(j) = (e_T - e_B)\left(\frac{1}{2} + \frac{j}{h}\right)^m + e_B \qquad (10)$$
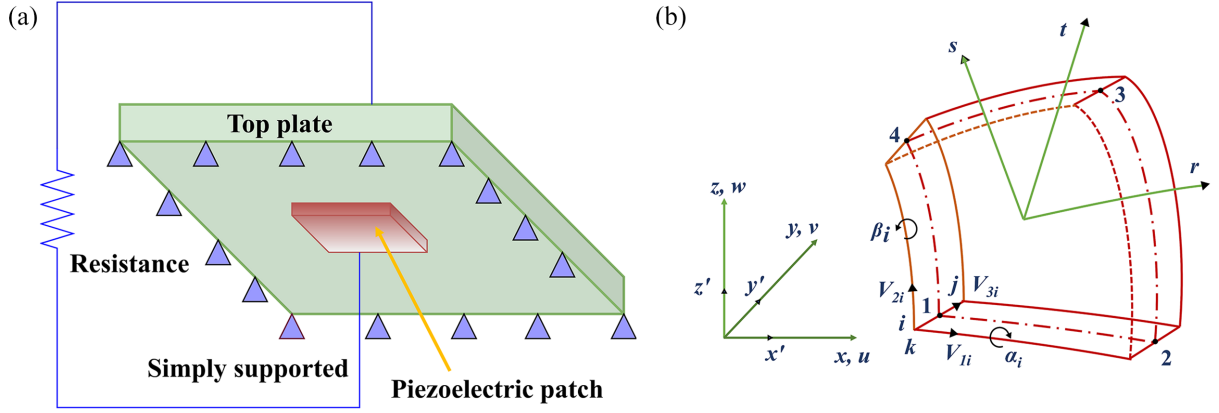
Figure 2. (a) Illustration of piezoelectric tile for energy harvesting application and (b) schematic diagram of four noded degenerated shell element.

$$\kappa(j) = (\kappa_T - \kappa_B)\left(\frac{1}{2} + \frac{j}{h}\right)^m + \kappa_B \tag{11}$$

$$\rho(j) = (\rho_T - \rho_B)\left(\frac{1}{2} + \frac{j}{h}\right)^m + \rho_B \tag{12}$$

$$Y(j) = (Y_T - Y_B)\left(\frac{1}{2} + \frac{j}{h}\right)^m + Y_B \tag{13}$$

Where e is the piezoelectric stress coefficient, κ is the material dielectric coefficient, ρ is the material density, and Y is the modulus of rigidity of the FG-GRPC. Properties of bottom and top layers from equation (10) to (13) are represented using subscripts B and T respectively.

2.3. Finite element formulation

The Finite Element Method is a computational method for analyzing the piezolaminated composite shell in order to design the structure's static and dynamic response. Finite element formulations facilitate the modeling of complicated geometries, resulting in a broad range of applications. Many studies employed finite element analysis to investigate the static and dynamic behaviors of piezolaminated shell structures (Adhikari et al., 2021; Bathe, 1996; Kumar et al., 2008). For structural modeling in this work, a four-noded isoparametric degenerated shell element with five degrees of freedom per node is utilized. The finite element approach is based on first order shear deformation theory and piezoelectric theory. The structure is supposed to move in a linear range. The piezoelectric layer is completely adhered to the tile, and the adhesive used has no effect on the structural characteristics. The tile's top plate is constructed from metal or composite material, while the piezoelectric patch is composed of functionally graded material or ceramics. For the energy harvesting application, the tile's upper surface and

piezoelectric patch are linked to an external resistance as shown in Figure 2(a).

2.3.1. Geometry and displacement field.
A degenerated shell element is used to convert a three-dimensional solid element to a two-dimensional element. The assumption is that the first two dimensions are substantially larger than the third, therefore the change in characteristics in the third direction may be ignored. Degenerated shell elements need far less computing time than solid elements, making them more cost efficient. Any arbitrary location (refer Figure 2(b)) in the structure can be described using nodal coordinates and thickness as (Kumar et al., 2008).

$$\begin{Bmatrix} x \\ y \\ z \end{Bmatrix} = \sum_{i=1}^{nel} N_i \left\{ \begin{Bmatrix} x_i \\ y_i \\ z_i \end{Bmatrix} + \frac{1}{2} t\, h_i \begin{Bmatrix} l_{3i} \\ m_{3i} \\ n_{3i} \end{Bmatrix} \right\} \tag{14}$$

where t is the natural coordinate along thickness direction, nel is the number of nodes per element, N_i is the shape function, and h_i is the nodal thickness. The midsurface of node i has x_i, y_i, and z_i as the global coordinates, and l_{3i}, m_{3i}, and n_{3i} are direction cosines of unit vector V_{3i}

The displacement field is specified in terms of five degrees of freedom, namely three translational components of displacements (u, v, and w) and two nodal rotations about V_{1i} and V_{2i} (α_i and β_i), based on assumptions of degenerated shell element.

$$\begin{Bmatrix} u \\ v \\ w \end{Bmatrix} = \sum_{i=1}^{nel} N_i \left\{ \begin{Bmatrix} u_i{}^0 \\ v_i{}^0 \\ w_i{}^0 \end{Bmatrix} + \frac{1}{2} t\, h_i \begin{bmatrix} l_{1i} & -l_{2i} \\ m_{1i} & -m_{2i} \\ n_{1i} & -n_{2i} \end{bmatrix} \begin{Bmatrix} \alpha_i \\ \beta_i \end{Bmatrix} \right\} \tag{15}$$

where l_{si}, m_{si}, and n_{si} are the direction cosines of the unit vector V_{si}, where s varies from 0 to 3 at the node i.

2.3.2. Constitutive equations. Electromechanical equations of linear piezoelectric material are mentioned as follows (Bathe, 1996; Mao and Zhang, 2018)

$$\{\sigma\} = [D]\{\varepsilon\} - [e]\{E\} \tag{16}$$

$$\{T\} = [e]\{\varepsilon\} + [\kappa]\{E\} \tag{17}$$

Where $\{\sigma\}, \{T\}, [\kappa]$, and $\{E\}$ are stress vector, electrical displacement, dielectric permittivity, and electric field, respectively. $[e], [D]$, and $\{\varepsilon\}$ are piezoelectric coefficient's matrix in stress charge form, reduced elastic matrix, and strain vector, respectively.

$$\begin{Bmatrix} \sigma_{xx} \\ \sigma_{yy} \\ \sigma_{xy} \\ \sigma_{yz} \\ \sigma_{xz} \end{Bmatrix} = \begin{bmatrix} C_{11} & C_{12} & 0 & 0 & 0 \\ C_{12} & C_{22} & 0 & 0 & 0 \\ 0 & 0 & C_{66} & 0 & 0 \\ 0 & 0 & 0 & C_{44} & 0 \\ 0 & 0 & 0 & 0 & C_{55} \end{bmatrix} \begin{Bmatrix} \varepsilon_{xx} \\ \varepsilon_{yy} \\ \gamma_{xy} \\ \gamma_{yz} \\ \gamma_{xz} \end{Bmatrix}$$
$$- \begin{bmatrix} 0 & 0 & e_{31} \\ 0 & 0 & e_{32} \\ 0 & 0 & 0 \\ 0 & e_{24} & 0 \\ e_{15} & 0 & 0 \end{bmatrix} \begin{Bmatrix} E_x \\ E_y \\ E_z \end{Bmatrix} \tag{18}$$

$$\begin{Bmatrix} T_x \\ T_y \\ T_z \end{Bmatrix} = \begin{bmatrix} 0 & 0 & 0 & 0 & e_{15} \\ 0 & 0 & 0 & e_{24} & 0 \\ e_{31} & e_{32} & 0 & 0 & 0 \end{bmatrix} \begin{Bmatrix} \varepsilon_{xx} \\ \varepsilon_{yy} \\ \gamma_{xy} \\ \gamma_{yz} \\ \gamma_{xz} \end{Bmatrix}$$
$$+ \begin{bmatrix} \kappa_{11} & 0 & 0 \\ 0 & \kappa_{22} & 0 \\ 0 & 0 & \kappa_{33} \end{bmatrix} \begin{Bmatrix} E_x \\ E_y \\ E_z \end{Bmatrix} \tag{19}$$

Where $C_{11} = C_{22} = \frac{Y_c}{1-\nu^2}$, $C_{12} = \frac{\nu Y_c}{1-\nu^2}$, $C_{44} = C_{55} = C_{66} = \frac{\nu Y_c}{2(1+\nu)}$

Elastic constitutive law or stress strain relationship is used to characterize mechanical behavior under the effect of external stimulus. The stress-strain correlation is described in the local coordinate system by

$$\{\sigma\}' = [D]\{\varepsilon'\} \tag{20}$$

Where $\{\varepsilon'\}$ and $\{\sigma\}'$ are the strain and stress components in the local coordinate system, respectively; $[D]$ is the material matrix of the structural shell.

In equation (20), the stress and strain in the local coordinate system are translated into a global system as

$$\{\sigma\} = [D_T]\{\varepsilon\} \tag{21}$$

Where $\{\sigma\}$ and $\{\varepsilon\}$ are the stress and strain in the global coordinate system respectively and $[D_T]$ is the transformed material stiffness matrix of the shell structure.

Using the Hamilton's principle, governing equation of degenerated shell element can be given by

$$\int_{t_2}^{t_1} (\delta T - \delta U + \delta W_{ext}) dt = 0 \tag{22}$$

where W_{ext}, t, T, and U are the external work done, time, kinetic energy, and potential energy, respectively. By simplifying the terms and substituting them with suitable expressions, we get the complete finite element expression for the system as follows:

$$[M_{uu}]\{\ddot{q}\} + [C_{uu}]\{\dot{q}\} + [K_{uu}]\{q\} + [K_{\phi u}]\{\phi\} = \{F_m\} \tag{23}$$

$$[K_{\phi u}]\{q\} + [K_{\phi\phi}]\{\phi\} = \{Q\} \tag{24}$$

where $[K_{uu}]$, $[M_{uu}]$, $[C_{uu}]$, $[K_{\phi\phi}]$, and $[K_{\phi u}]$ are the stiffness matrix, global mass matrix, damping coefficient matrix, electrical stiffness matrix, and electromechanical stiffness matrix, respectively. $\{Q\}$ and $\{F_m\}$ are the electric charge vector and mechanical force vector, respectively.

According to circuit theory, the current flow through the resistance in terms of charge Q and voltage ϕ are given by:

$$i = -\frac{dQ}{dt} \tag{25}$$

$$i = \frac{\phi}{R} \tag{26}$$

Differentiating equation (24) and then using equation (25) and (26) to solve further, we get

$$\frac{d}{dt}\left([K_{\phi u}]\{q\} + [K_{\phi\phi}]\{\phi\}\right) = \frac{d\{Q\}}{dt} \tag{27}$$

$$[K_{\phi u}]\{\dot{q}\} + [K_{\phi\phi}]\{\dot{\phi}\} = -\frac{\{V\}}{R} \tag{28}$$

$$[K_{\phi u}]\{\dot{q}\} + [K_{\phi\phi}]\{\dot{\phi}\} + \frac{\{V\}}{R} = 0 \tag{29}$$

Power of the piezoelectric energy harvesting tile across the resistance R is given as

$$P = \frac{V^2}{R} \tag{30}$$

3. Results and discussion

3.1. Validation studies

Validation studies are carried out to assess the dependability, reliability, and accuracy of research results. The dependability of the formulation provided in the previous section is evaluated by replicating Nestorovic's results (Nestorović et al., 2012). The dimensions of a clamped
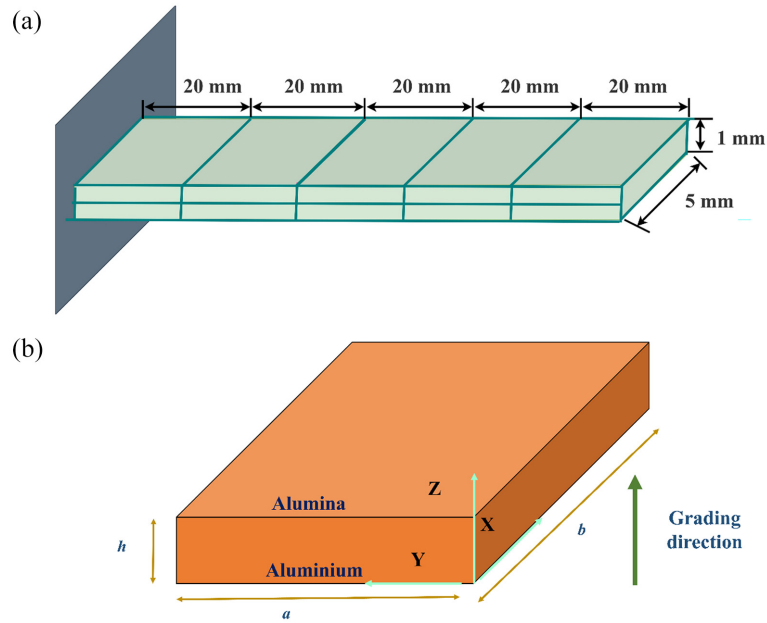
Figure 3. (a) Geometry of the cantilevered beam used for the validation and (b) simply supported functionally graded plate taken from Thai and Choi to be used in validation (Thai and Choi, 2013).

Table 1. Sensor voltage generated at various segments in PVDF bimorph beam.

Distance from fixed end (mm)	0–20 Sensor 1	20–40 Sensor 2	40–60 Sensor 3	60–80 Sensor 4	80–100 Sensor 5
Analytical (Nestorović et al., 2012)	293.24	229.62	163.85	98.31	35.51
ABAQUS (Nestorović et al., 2012)	295.2	229.6	164.02	98.42	32.8
Present	297.4	230	163.2	97.33	32.32

Table 2. Deflection ($\times 10^{-7}$ m) attained at various distances from fixed end for PVDF bimorph beam.

Distance from the fixed end (mm)	20	40	60	80	100
Analytical (Nestorović et al., 2012)	0.138	0.552	1.242	2.208	3.450
ABAQUS (Nestorović et al., 2012)	0.138	0.552	1.242	2.208	3.450
ANSYS (Nestorović et al., 2012)	0.138	0.551	1.239	2.203	3.441
Present	0.138	0.552	1.242	2.208	3.449

bimorph beam are 100 mm in length, 5 mm in width, and 1 mm in thickness. Figure 3(a) illustrates the discretization of the piezoelectric bimorph made of PVDF into five elements. The tip is deflected by 0.01 m to acquire sensor voltage at various segment lengths, as specified in Table 1. The geometric and material properties features are retained in the way stated in the reference. For the actuation validation, a voltage of 1 V is provided throughout the length of the beam. Table 2 compares the collected data to previously reported data.

Another validation is carried out by repeating Thai and Choi's findings (Thai and Choi, 2013). Figure 3(b) shows a functionally graded material plate of aluminum and aluminum oxide (alumina) with squared sides of

1 mm. Aluminum and alumina have moduli of elasticity of 70 and 380 GPa, respectively. A sinusoidally varying force of 1 N/m^2 is applied to the FGM layer to achieve the necessary mechanical validation. The numerical results are obtained using simply supported boundary conditions, with a length-to-thickness ratio of 10. Other material and geometric factors are kept consistent with the reference. Table 3 details the contrast between the reference and the current research.

3.2. Numerical studies

This section will examine the interaction of graphene platelets with piezoelectric materials, namely BaTiO$_3$

Table 3. Comparison of the present research to that of Thai and Choi (2013).

	Positions (x, y, z)	Thai and Choi (2013)	Current study
Deflection Z (w)	$\left(\frac{l}{2}, \frac{b}{2}\right)$	1.1909	1.1907
Stress X(σ_x)	$\left(\frac{l}{2}, \frac{b}{2}, \frac{h}{2}\right)$	5.1853	5.202
Stress Y(σ_y)	$\left(\frac{l}{2}, \frac{b}{2}, \frac{h}{3}\right)$	2.0441	2.0431
Stress XY (σ_{xy})	$\left(\frac{l}{2}, \frac{b}{2}, -\frac{h}{3}\right)$	0.9998	0.9981
Stress YZ (σ_{yz})	$\left(\frac{l}{2}, \frac{b}{2}, \frac{h}{6}\right)$	0.4799	0.4921
Stress XZ (σ_{xz})	$\left(\frac{l}{2}, \frac{b}{2}, 0\right)$	0.3407	0.3601

and PVDF; functionally grade both materials; and finally, evaluate the consolidated circuit performance owing to coalescence of material grading and graphene platelets. In order to accomplish this, a MATLAB algorithm based on finite element formulation is created for harvesting energy from FG-GRPC tiles. The energy harvesting of FG-GRPC tile when exposed to electromechanical loading is investigated in this section. This FG-GRPC tile is made of two GRPC materials that have been functionally graded along thickness direction. The first GRPC material in our analysis is GRPC-BT, which is constituted of GPLs nanofillers reinforced in a $BaTiO_3$ piezoelectric matrix. The second GRPC material, identified as GRPC-PV, is composed of GPLs nanofillers reinforced in a PVDF piezoelectric matrix. Table 4 shows the electromechanical characteristics of both piezoelectric materials. The HT and ROM are used to compute the effective electromechanical characteristics of both GRPC materials. According to the experimental investigations in literature, the volume percentage of GPLs is maintained below or equal to 1% due to the possibility of agglomeration (Mao and Zhang, 2018). The rectangular GPLs utilized in the study had a length (l_{gpl}), width (b_{gpl}), and thickness (t_{gpl}) of 2.5 μm, 1.5 μm, and 1.5 nm, respectively. Graphene has an elastic modulus of 1010 GPa, a poisson's ratio of 0.186, and density of 800 kg/m³ respectively (Layek et al., 2010;

Song et al., 2020). Additionally, several experimental studies have shown that graphenes have a strong piezoconductive effect that is proportional to the amount of graphene and its layers. In this case, we assume that the piezoelectric characteristics of the GPLs are α times larger than those of barium titanate and PVDF, namely, $e_{31,G} = \alpha e_{31,M}$, $e_{32,G} = \alpha e_{32,M}$, $e_{24,G} = \alpha e_{24,M}$, $e_{15,G} = \alpha e_{15,M}$, $\kappa_{11,G} = \alpha \kappa_{11,M}$, $\kappa_{22,G} = \alpha \kappa_{22,M}$, and $\kappa_{33,G} = \alpha \kappa_{33,M}$ (Mao and Zhang, 2018). We refer this α as the piezoelectric multiple. The effective properties of stiffness coefficient, density, piezoelectric coefficient, and electrical permittivity against the GPLs volume fraction (V_{gpl}) for GRPC-BT material are illustrated in Figure 4(a) to (d). It can be deduced that as the value of V_{gpl} increases, the electromechanical characteristics of GRPC structures improve significantly. The piezoelectric stress coefficient rises from −4.4 C/m² to −74.76 C/m², a 16-fold improvement over the original values. This substantial improvement comes as a linear variation and is attributed to the excellent electromechanical characteristics of GPLs nanofillers. Similarly, a major increase in all mechanical and electrical characteristics is seen in the second GRPC material containing PVDF matrix, as illustrated in Figure 5(a) to (d).

As previously stated, the FG-GRPC is comprised of two GRPC materials whose properties vary according to the simple power distribution law provided by equations (10)–(13). In the present work, two GRPC materials with $BaTiO_3$ and PVDF as matrix composites are developed, and these two are functionally graded along the thickness to form FG-GRPC tile. The FG-GRPC is constructed such that the bottom surface is GRPC-BT and the top surface is GRPC-PV. Figure 6 depicts the variation of density and relative permittivity for various values of grading index m to highlight this power-law variation in FG-GRPC. It can be seen that at m = 0, the material is completely infused with GRPC-PV properties, with a density of 1778 kg/m³ and a piezoelectric coefficient (e_{31}) of −0.5457 C/m², whereas at m = ∞, the material is completely infused with GRPC-BT properties, with a density of 5690 kg/m³ and a piezoelectric coefficient (e_{31}) of −18.47 C/m². The GRPC-PV and GRPC-BT property values mentioned above are obtained at GPL volume fraction, V_{gpl} = 0.2 %.

Table 4. Specification of the materials used in the current analysis.

Material	BaTiO₃ (Hussein and Heyliger, 1998; Ramirez et al., 2006)	PVDF (Mao and Zhang, 2018, 2019; Ramirez et al., 2006)
Young's modulus (GPa)	118	2
Poisson's ratio	0.35	0.3
Density (kg/m³)	5700	1920
Piezoelectric coefficient, e_{31} (C/m²)	−4.4	−0.13
Piezoelectric coefficient, e_{33} (C/m²)	18.6	−0.28
Relative permittivity, κ_{33}	1450	12
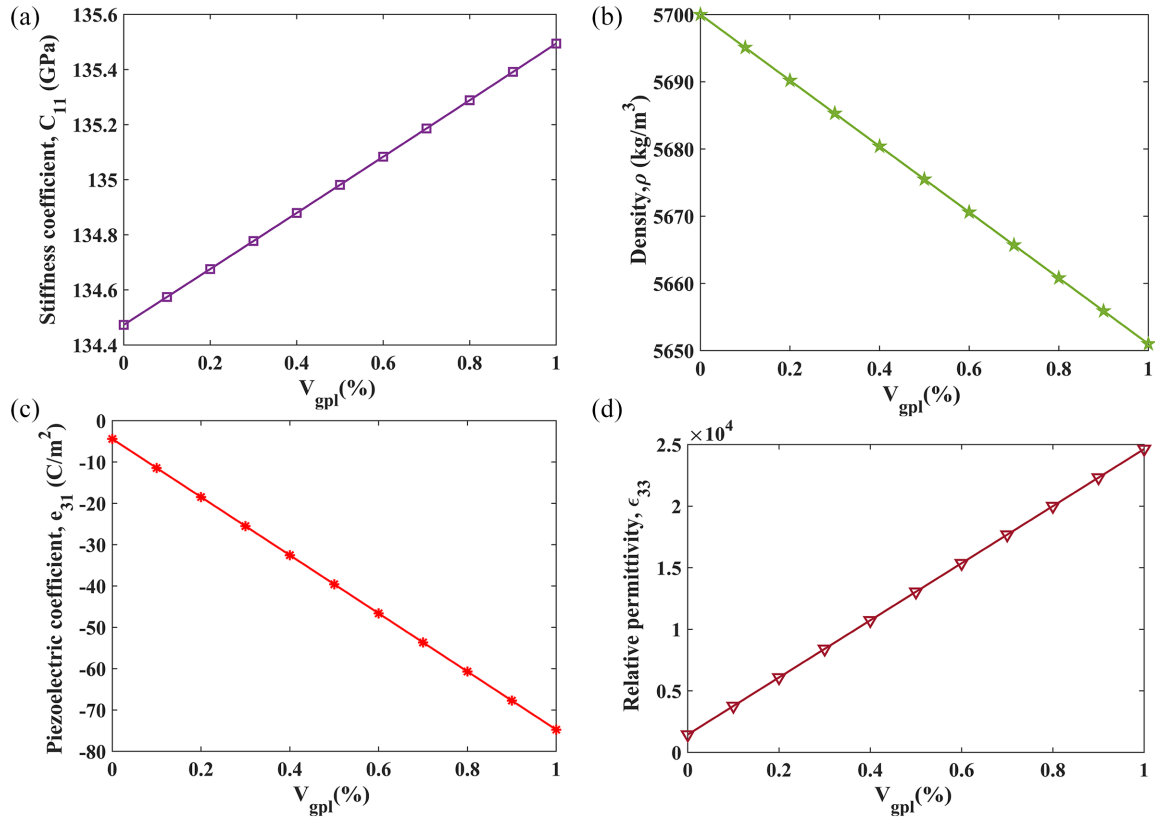
Figure 4. Influence of GPL volume fraction (V_{gpl}) on different properties of BaTiO$_3$: (a) stiffness coefficient, (b) density, (c) piezoelectric stress coefficient, and (d) relative electrical permittivity.

After the FG-GRPC material is developed, an electromechanical analysis is conducted to determine the circuit metrics, namely voltage and power. This is accomplished by using a simply supported tile (SSSS), which is comprised of platinum (modulus of rigidity, $E = 154$ GPa, density $\rho = 21{,}450$ kg/m^3, and poisson's ratio, $\nu = 0.3$) as the top plate and has a side of 150 mm, as shown in Figure 7. The piezoelectric patch at the bottom is FG-GRPC comprised of GRPC-BT and GRPC-PV. All simulation investigations in this paper are conducted on a FG-GRPC square sample with sides of 10 mm. The FG-GRPC and platinum top plate have a fixed thickness of 1 mm. The boundary load is applied in the form of tension on the top plate with a magnitude of 50 N.

The patch position, on the other hand, must be established for maximum piezoelectric efficiency. Four cases are examined using FG-GRPC placed on platinum using a variety of patch centers, as illustrated in Figure 8(a). The circuit performance of each of the four scenarios is determined in terms of voltage, as seen in Figure 8(b). It is obvious that the highest performance efficiency is obtained when the patch is mounted in the tile's center. This is because the SSSS boundary condition generates a large strain energy density at the center point. As a result, the FG-GRPC patch will be placed

in the center for any further simulation studies in the current research.

Next, interaction between various parameters is assessed to ascertain their influence on the tile's efficiency. The impact of external resistance on circuit metrics at various frequency levels under electromechanical loading is shown in Figure 9. It is worth noting that the same $V_{gpl}(\%)$ is used to form GRPC-PV and GRPC-BT prior to functionally grading them. The voltage rises in proportion to the resistance value and then remains constant after the peak is achieved. This is because voltage and resistance have a proportional relationship. However, generated power exhibits a different pattern toward resistance change. The power value initially rises, but after reaching a peak, it decreases as the load resistance increases. The initial gain is caused by an increase in voltage, but as resistance rises, power falls owing to their inverse proportional relation. For instance, power increases from 0.01 mW at 10 kΩ to 1.967 mW at 0.41 MΩ before declining to 0.157 mW at 9 MΩ. The maximum power output is 1.967 mW and is achieved at 0.41 MΩ and 12 Hz, for $V_{gpl} = 0.5\%$. However, these maximum power and voltage levels are dependent on the frequency and load resistance. The higher the frequency, the less load resistance is required to achieve the peak power. For example, maximum
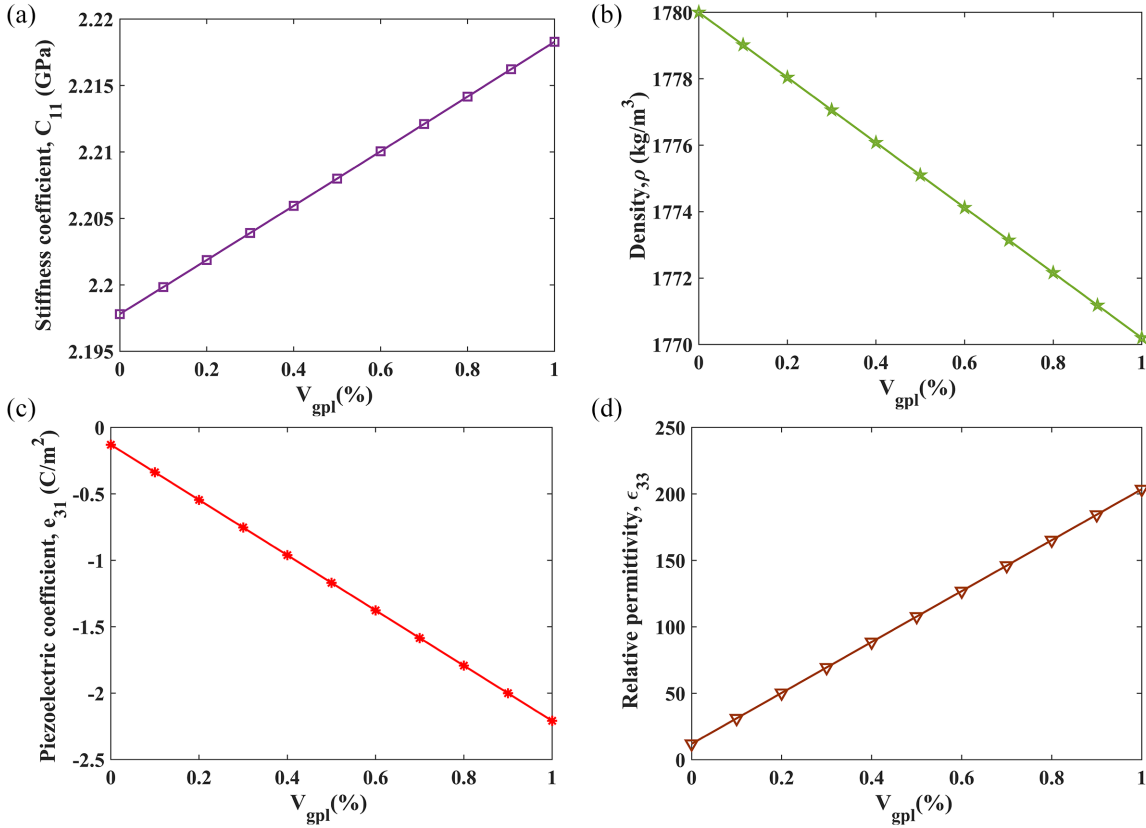
Figure 5. Influence of GPL volume fraction (V_{gpl}) on different properties of PVDF: (a) stiffness coefficient, (b) density, (c) piezoelectric stress coefficient, and (d) relative electrical permittivity.
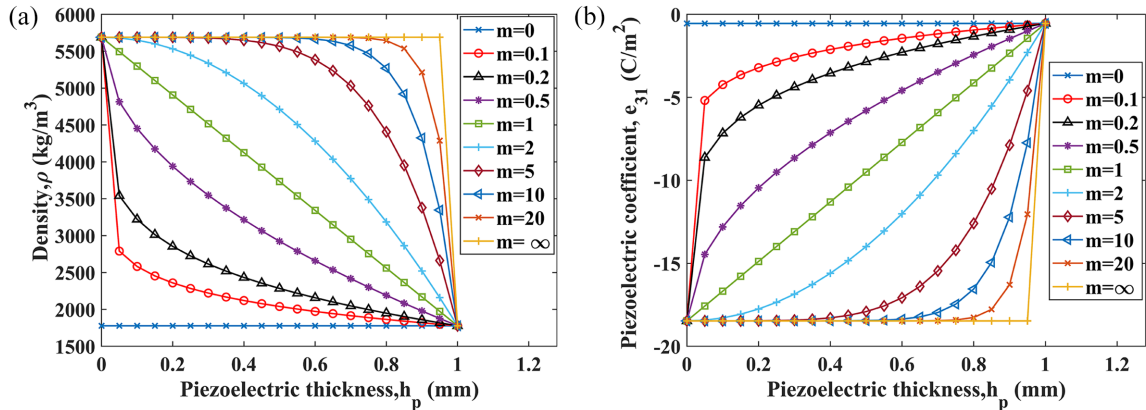
Figure 6. Spatial variation of (a) density and (b) relative permittivity across height of the piezoelectric material for various values of grading index m at $V_{gpl} = 0.2$.

power is attained at 0.41 MΩ for 12 Hz, whereas 2 MΩ is required for 2 Hz. The reason for this behavior is that maximal power transfer happens once the optimal resistance condition, $R_{opt} = 1/(C_p.2\pi f)$ (Kim et al., 2004) is met. It is obvious from the formula that both capacitance (C_p) and frequency (f) are negatively related to optimal resistance. A similar trend can be seen among generated voltage, frequency, and resistance.

Following that, the frequency response of the FG-GRPC tile is evaluated utilizing thickness values ranging from 0.05 to 1.5 mm as described in Figure 10. It is apparent that increasing the frequency has a beneficial influence on both parameters' performance. The noteworthy conclusion is the output voltage and power's non-uniform response to changes in piezoelectric thickness. The circuit metrics first rise as the piezoelectric
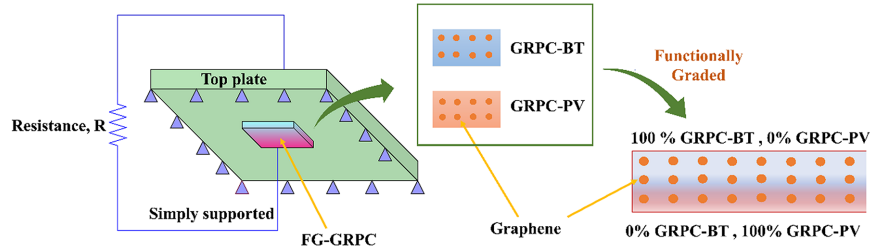
Figure 7. Illustration of simply supported tile with attached FG-GRPC patch.
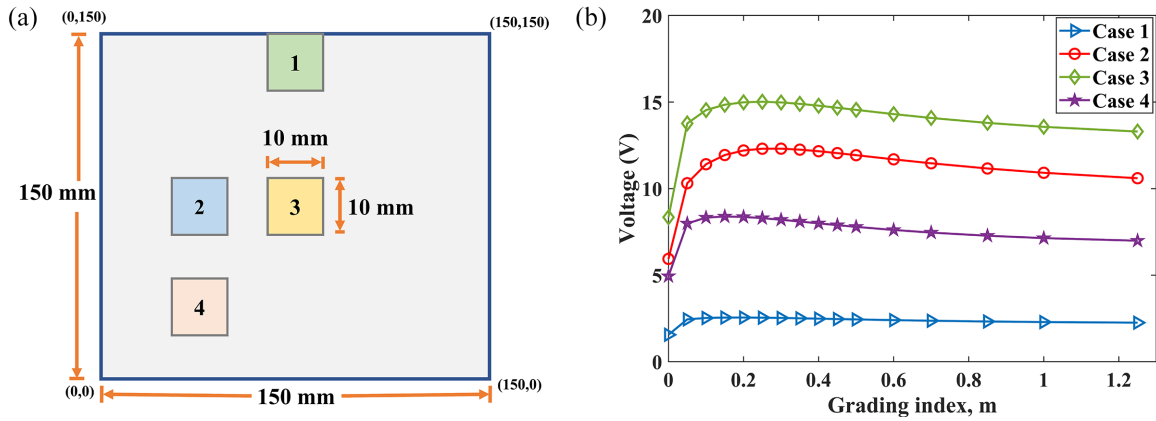
Figure 8. (a) Location of piezoelectric patch for different cases along with patch centers (x_c mm, y_c mm): Case 1- Top Mid (75, 150), Case 2- Mid left (37.5, 75), Case 3- Center (75, 75), Case 4- Diagonal (37.5, 37.5) and (b) line graph depicting the relationship between material grading index and voltage for the four cases.
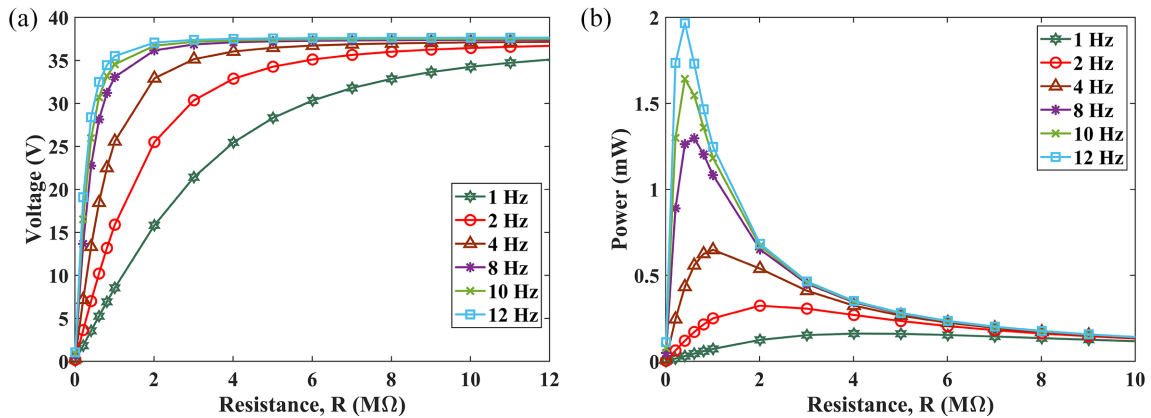
Figure 9. Influence of external resistance on output (a) voltage (b) power at discrete frequency values.

height rises, then plateau at $h_p = 1$ mm and subsequently decrease till the end. The initial gain is related to an increase in the volume of piezoelectric material, but excessive thickness enables stiffness to grow, leading in a subsequent fall.

The influence of variation in the piezoelectric side (a_p) and external resistance, R on circuit metrics is then investigated at a frequency of 1 Hz. For practically any value of external resistance, the voltage and power increase as the magnitude of the piezoelectric side

increases, as illustrated in the Figure 11. This is because increasing the piezoelectric side increases the overall volume of piezoelectric material. For instance, at resistance of 200 kΩ, the voltage and power increases from 4.019 V and 0.0769 mW to 5.298 V and 0.1357 mW, resulting in 31.82% and 76.46% rise in performance enhancement as a_p changes from 8 mm to 13 mm.

Next, the change in voltage response may be interpreted by analyzing the volume fraction distribution of the elements across the height in Figure 12(a). At
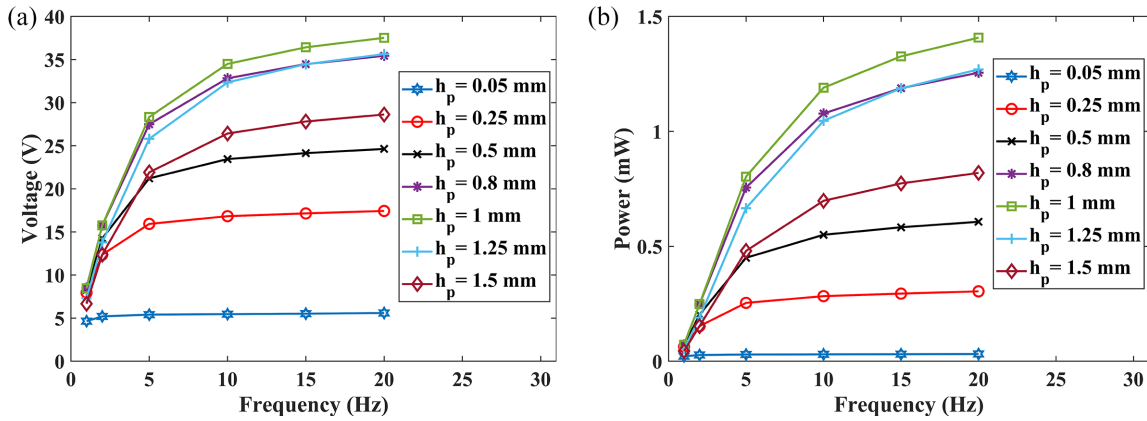
Figure 10. Frequency response curves for (a) voltage and (b) power at various values of piezoelectric thickness using platinum substrate.
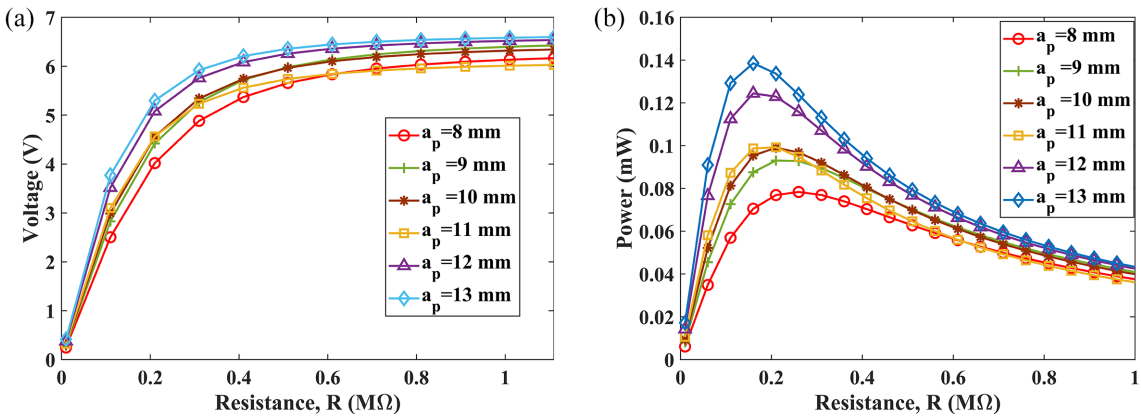
Figure 11. (a) Output voltage and (b) power as a function of external resistance at different values of piezoelectric side.
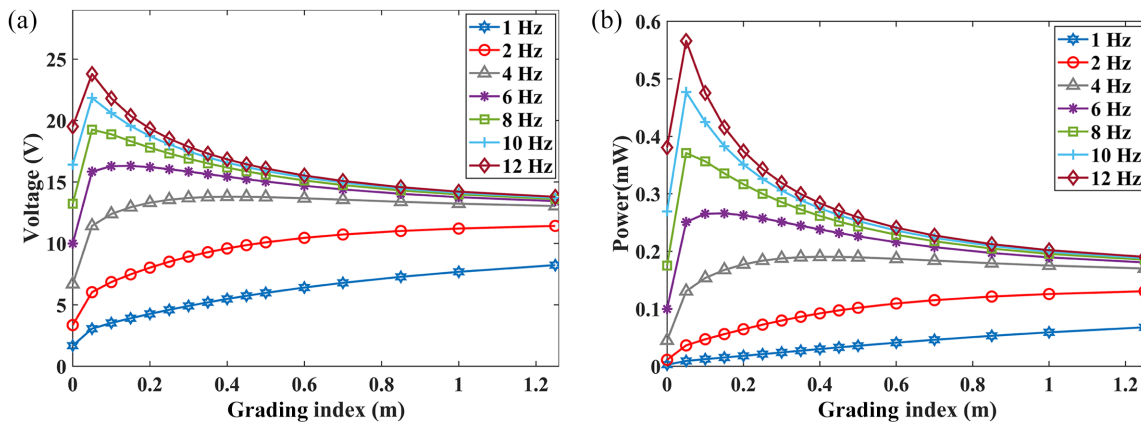
Figure 12. Effect of material grading exponent on (a) voltage and (b) power at different values of frequency.

$m = 0$ and $f = 6$ Hz, the piezoelectric material is completely enriched with GRPC-PV properties having PVDF matrix, generating a voltage of 9.989 V. Consequently, voltage increases to 15.84 V at grading index $m = 0.05$. This is due to the patch's piezoelectric properties from GRPC-BT, which contains BaTiO$_3$.

The maximum voltage of 16.29 V is achieved at grading index, $m = 0.1$. This is owing to the fact that the piezoelectric layer has maximal strain and low piezoelectric magnitude at $m = 0$, as it only contains PVDF matrix. However, as the grading index increases, the patch loses its strain property and acquires BaTiO$_3$
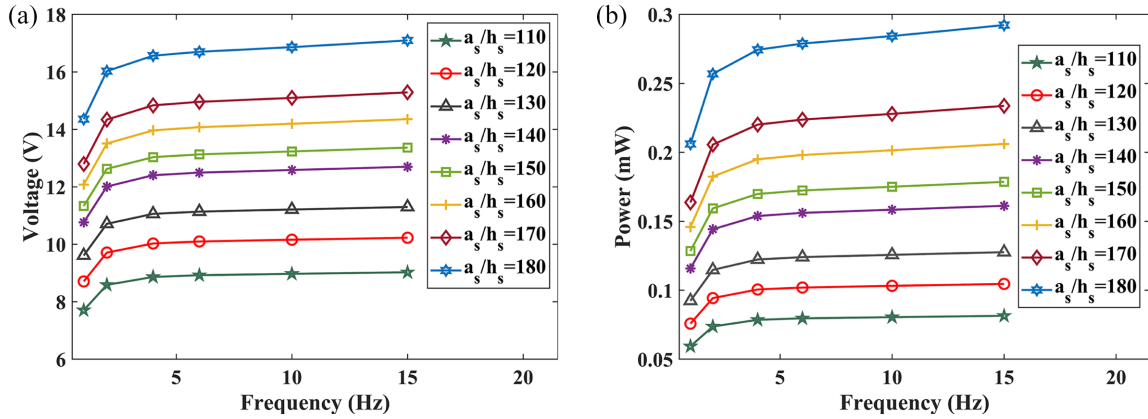
Figure 13. Influence of side to thickness ratio of substrate layer for different frequency response curves of (a) voltage and (b) power.
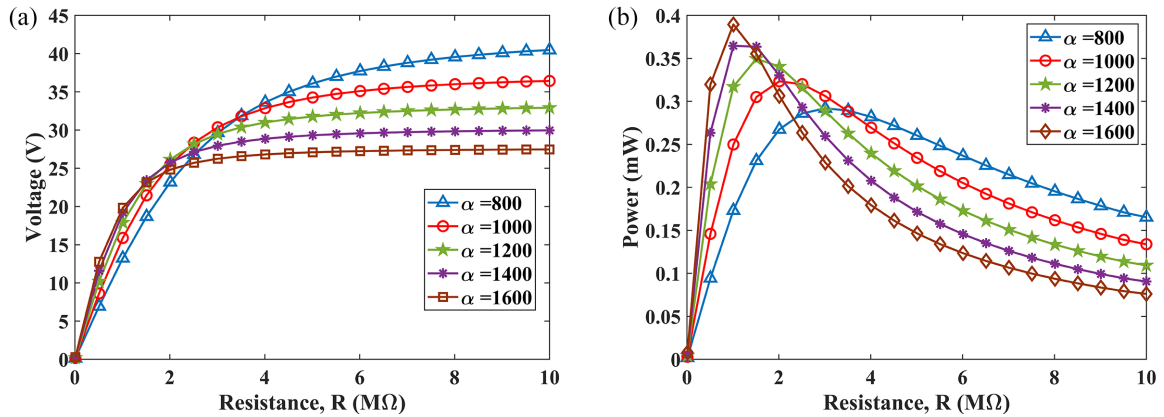
Figure 14. Influence of external resistance on (a) voltage and (b) power at different values of piezoelectric multiple, α.

piezoelectric contribution from GRPC-BT. The piezoelectric layer stiffens as m increases ($m \geq 0.1$), resulting in a reduced output voltage owing to decreased strains. Because of the highest voltage values at $m = 0.1$, it can be referred to as the optimized grading index for frequency of 6 Hz. For grading index, $m \geq 1.2$, the results stay the same and may therefore be considered as values of fully GRPC-BT material. The output voltage for FG- GRPC at this grading index of 1.2 is 13.44 V. Thus, the voltage at optimized grading index for a frequency of 6 Hz represents a ~17.5% increase over the voltage at pure GRPC-BT piezoelectric material. However, the maximum voltage and power are 23.79 V and 0.566 mW which are attained at a frequency of 12 Hz. It is worth mentioning that the highest percentage gains in performance for voltage and power are 44.30%, and ~105.25%, respectively, achieved at frequency of 8 Hz. Additionally, as illustrated in Figure 12, the optimized grading index differs according to the frequency value. The synergetic impact of the piezoelectric, dielectric, and mechanical characteristics of both phases of FG-GRPC is

responsible for this astonishing improvement in piezoelectric performance.

Figure 13 depicts the effect of side to thickness ratio (STR) on the circuit metrics. The frequency curves are plotted in range of 0–15 Hz under the external resistance of 1 MΩ. The STR variation is taken in such a way that the area between them remains constant. Voltage and power output increases with rise in STR for any frequency value. At frequency of 15 Hz, the voltage increases from 9.025 to 17.1 V resulting in 90% increase as STR changes from 110 to 180. In similar STR variation, power increases from 0.081 to 0.2923 mW mounting to 260% increment. This is due to the fact that with increase in STR value, the thickness keeps on decreasing with respect to side as the area remains constant. The reduced thickness helps in better mechanical energy transmission ratio mounting to better performance results.

Figure 14 plots the influence of the piezoelectric multiple α on the (a) voltage and (b) power change with external resistance at $V_{gpl} = 0.50\%$. Initially, up till 2.25 MΩ the voltage remains almost the same for

different α values ranging from 800 to 1600. However, after that every α shows the deviation and an inversely proportional relationship is maintained. Contrarily, the power interaction with piezoelectric multiple (α) is an interesting one as maximum peak value of power is achieved at maximum α = 1600. However, after 4 MΩ resistance, a similar pattern as that of voltage is observed that is a negative relation of power with α increase. However, owing to an overreliance on other variables such as resistance, a tangible relationship between them cannot be drawn.

4. Conclusion

This article comprehensively presents the electromechanical response of a smart composite functionally graded tile reinforced by GPLs utilizing first order shear deformation theory and Hamilton's principle. The HT approach is used to determine the effective characteristics of the modulus of elasticity and stiffness matrices of two-lead free graphene induced materials, namely $BaTiO_3$ and PVDF. The additional mechanical and electrical characteristics of graphene induced $BaTiO_3$ (GRPC-BT) and PVDF (GRPC-PV) are calculated using the ROM model. It was discovered that the effective characteristics of GPLs, such as elastic modulus, piezoelectric coefficient, and electrical permittivity increase as the volume percentage of GPLs rises. It is owing to the strong electromechanical properties of GPLs. Following that, both reinforced composites are functionally graded using a simple power law distribution to vary the characteristics, resulting in the lead-free FG-GRPC tile. A parametric analysis is used to evaluate the influence of piezoelectric side and height, STR, frequency, external resistance, material grading index, and piezoelectric multiple α on the circuit metrics, namely voltage and power. It has been observed that increasing the piezoelectric side, frequency, and STR improves circuit metrics. However, piezoelectric height has an initial beneficial impact on performance until it reaches a peak and then gradually decreases till the end. Additionally, a tangible relationship between piezoelectric multiple and circuit metrics cannot be established owing to their reliance on other external characteristics. Besides, the material grading index parameter contributes to performance enhancement and its optimal value is frequency sensitive. At a frequency of 8 Hz, the maximum performance enhancements for voltage and power are 44.30% and 105.25%, respectively. The synergetic impact of the piezoelectric, dielectric, and mechanical characteristics of both GRPC-BT and GRPC-PV portions is responsible for this remarkable increase in piezoelectric structure performance. The findings clearly demonstrate the enormous potential for developing future smart structures via the use of GPLs and material compositional grading.

ORCID iD

Jitendra Adhikari (iD) https://orcid.org/0000-0001-9728-5644

References

Adhikari J, Kumar A, Kumar R, et al. (2021) Performance enhancement of functionally graded piezoelectric tile by tailoring poling orientation. *Mechanics Based Design of Structures and Machines* 0(0): 1–20.

Adhikari J, Kumar R and Jain SC (2022) Angular poling effect on cymbal piezoelectric structure using rhombohedral and tetragonal PMN-0.33PT for energy harvesting applications. *Applied Physics A* 128(5): 122.

Agnolucci P (2007) Economics and market prospects of portable fuel cells☆. *International Journal of Hydrogen Energy* 32(17): 4319–4328.

Bathe KJ (1996) *Finite Element Procedures*. Englewood Cliffs, NJ: Prentice Hall.

Feng C, Kitipornchai S and Yang J (2017) Nonlinear bending of polymer nanocomposite beams reinforced with non-uniformly distributed graphene platelets (GPLs). *Composites Part B Engineering* 110: 132–140.

Geim AK and Novoselov KS (2010) The rise of graphene. In: Rodgers P (ed.) *Nanoscience and Technology: A Collection of Reviews From Nature Journals*. Singapore: World Scientific. pp.11–19.

Gholami R and Ansari R (2018) Nonlinear harmonically excited vibration of third-order shear deformable functionally graded graphene platelet-reinforced composite rectangular plates. *Engineering Structures* 156: 197–209. November 2017.

He XQ, Liew KM, Ng TY, et al. (2002) A FEM model for the active control of curved FGM shells using piezoelectric sensor/actuator layers. *International Journal for Numerical Methods in Engineering* 54(6): 853–870.

He XQ, Ng TY, Sivashanker S, et al. (2001) Active control of FGM plates with integrated piezoelectric sensors and actuators. *International Journal of Solids and Structures* 38(9): 1641–1655.

Hussein M and Heyliger P (1998) Three-dimensional vibrations of layered piezoelectric cylinders. *Journal of Engineering Mechanics* 124(11): 1294–1298.

Kim HW, Batra A, Priya S, et al. (2004) Energy harvesting using a piezoelectric "cymbal" transducer in dynamic

environment. *Japanese Journal of Applied Physics* 43(9R): 6178.

Kumar R, Mishra BK and Jain SC (2008) Static and dynamic analysis of smart cylindrical shell. *Finite Elements in Analysis and Design* 45(1): 13–24.

Kumar S, Singh TP, Kumar R, et al. (2022) Experiment and parametric analysis of sliding mode triboelectric energy harvester. *Mechanics Based Design of Structures and Machines* 0(0): 1–15.

Layek RK, Samanta S, Chatterjee DP, et al. (2010) Physical and mechanical properties of poly(methyl methacrylate) - functionalized graphene/poly(vinylidine fluoride) nanocomposites: Piezoelectric β polymorph formation. *Polymer* 51(24): 5846–5856.

Lu W, Weng J, Wu D, et al. (2006) Epoxy resin/graphite electrically conductive nanosheet nanocomposite. *Materials and Manufacturing Processes* 21(2): 167–171.

Malekzadeh P and Alibeygi Beni A (2010) Free vibration of functionally graded arbitrary straight-sided quadrilateral plates in thermal environment. *Composite Structures* 92(11): 2758–2767.

Mao JJ and Zhang W (2018) Linear and nonlinear free and forced vibrations of graphene reinforced piezoelectric composite plate under external voltage excitation. *Composite Structures* 203: 551–565. May.

Mao JJ and Zhang W (2019) Buckling and post-buckling analyses of functionally graded graphene reinforced piezoelectric plate subjected to electric potential and axial forces. *Composite Structures* 216: 392–405. March.

Nestorović T, Marinković D, Chandrashekar G, et al. (2012) Implementation of a user defined piezoelectric shell element for analysis of active structures. *Finite Elements in Analysis and Design* 52: 11–22.

Rafiee MA, Rafiee J, Wang Z, et al. (2009) Enhanced mechanical properties of nanocomposites at low graphene content. *ACS Nano* 3(12): 3884–3890.

Ramirez F, Heyliger PR and Pan E (2006) Free vibration response of two-dimensional magneto-electro-elastic laminated plates. *Journal of Sound and Vibration* 292(3–5): 626–644.

Roque CM, Ferreira AJ and Jorge RM (2007) A radial basis function approach for the free vibration analysis of functionally graded plates using a refined theory. *Journal of Sound and Vibration* 300(3-5): 1048–1070.

Rout M, Hota SS and Karmakar A (2019) Thermoelastic free vibration response of graphene reinforced laminated composite shells. *Engineering Structures* 178: 179–190. October 2018.

Sahmani S and Aghdam MM (2017) Nonlinear instability of axially loaded functionally graded multilayer graphene platelet-reinforced nanoshells based on nonlocal strain gradient elasticity theory. *International Journal of Mechanical Sciences* 131-132: 95–106. June.

Sankar BV (2001) An elasticity solution for functionally graded beams. *Composites Science and Technology* 61(5): 689–696.

Shen HS, Xiang Y, Fan Y, et al. (2018) Nonlinear vibration of functionally graded graphene-reinforced composite laminated cylindrical panels resting on elastic foundations in thermal environments. *Composites Part B Engineering* 136: 177–186. September 2017.

Shi Q, Dong B, He T, et al. (2020) Progress in wearable electronics/photonics—Moving toward the era of artificial intelligence and internet of things. *InfoMat* 2(6): 1131–1162.

Shirvanimoghaddam M, Shirvanimoghaddam K, Abolhasani MM, et al. (2019) Towards a green and self-powered Internet of things using piezoelectric energy harvesting. *IEEE Access* 7: 94533–94556.

Singh K, Sharma S, Talha M, et al. (2021) A 3-Dimensional approach for evaluating the influence of poling orientation on piezoelectric characteristics. *Journal of Electronic Materials* 50(10): 5846–5856.

Song M, Gong Y, Yang J, et al. (2020) Nonlinear free vibration of cracked functionally graded graphene plateletreinforced nanocomposite beams in thermal environments. *Journal of Sound and Vibration* 468: 468–115115.

Song M, Yang J, Kitipornchai S, et al. (2017) Buckling and postbuckling of biaxially compressed functionally graded multilayer graphene nanoplatelet-reinforced polymer composite plates. *International Journal of Mechanical Sciences* 131-132: 345–355. April.

Song M, Zhou L, Karunasena W, et al. (2022) Nonlinear dynamic instability of edge-cracked functionally graded graphene-reinforced composite beams. *Nonlinear Dynamics* 109(4): 1–19.

Song X, Peng C, Peng S, et al. (2020) Unit commitment optimization model of wind storage combined system considering peak load regulation of energy storage system. *Proceedings - 2020 International Conference on Intelligent Transportation, Big Data and Smart City*, ICITBS 2020, 468–472.

Sundararajan N, Prakash T and Ganapathi M (2005) Nonlinear free flexural vibrations of functionally graded rectangular and skew plates under thermal environments. *Finite Elements in Analysis and Design* 42(2): 152–168.

Thai HT and Choi DH (2013) A simple first-order shear deformation theory for the bending and free vibration analysis of functionally graded plates. *Composite Structures* 101: 332–340.

Tien JM (2017) Internet of things, real-time decision making, and Artificial Intelligence. *Annals of Data Science* 4(2): 149–178.

Vel SS and Batra RC (2000) Three-dimensional analytical solution for hybrid multilayered piezoelectric plates. *Journal of Applied Mechanics* 67(3): 558–567.

Wang KF and Wang BL (2018) A mechanical degradation model for bidirectional natural fiber reinforced composites under hydrothermal ageing and applying in buckling and vibration analysis. *Composite Structures* 206: 594–600. August.

Wang YQ, Ye C and Zu JW (2019) Nonlinear vibration of metal foam cylindrical shells reinforced with graphene platelets. *Aerospace Science and Technology* 85: 359–370.

Wu H, Li Y, Li L, et al. (2022) Free vibration analysis of functionally graded graphene nanocomposite beams partially in contact with fluid. *Composite Structures* 291: 291–115609.

Wu H, Yang J and Kitipornchai S (2018) Parametric instability of thermo-mechanically loaded functionally graded graphene reinforced nanocomposite plates. *International Journal of Mechanical Sciences* 135: 431–440. November 2017.

Yang B, Kitipornchai S, Yang YF, et al. (2017) 3D thermo-mechanical bending solution of functionally graded graphene reinforced circular and annular plates. _Applied Mathematical Modelling_ 49: 69–86.

Yang B, Mei J, Chen D, et al. (2018) 3D thermo-mechanical solution of transversely isotropic and functionally graded graphene reinforced elliptical plates. _Composite Structures_ 184: 1040–1048. September 2017.

Zaman I, Phan TT, Kuan HC, et al. (2011) Epoxy/graphene platelets nanocomposites with two levels of interface strength. _Polymer_ 52(7): 1603–1611.

Zhang W, Niu Y and Behdinan K (2020) Vibration characteristics of rotating pretwisted composite tapered blade with graphene coating layers. _Aerospace Science and Technology_ 98: 105644.

Zhao Z, Feng C, Wang Y, et al. (2017) Bending and vibration analysis of functionally graded trapezoidal nanocomposite plates reinforced with graphene nanoplatelets (GPLs). _Composite Structures_ 180: 799–808.

Zhu B, Dong Y and Li Y (2018) Nonlinear dynamics of a viscoelastic sandwich beam with parametric excitations and internal resonance. _Nonlinear Dynamics_ 94(4): 2575–2612.